DNS STUDY OF TURBULENT HEAT TRANSFER IN A SPANWISE ROTATING SQUARE DUCT

Bing-Chen Wang

Department of Mechanical Engineering
University of Manitoba
Winnipeg, MB, R3T 5V6, Canada
BingChen.Wang@umanitoba.ca

Xingjun Fang

Department of Mechanical Engineering
University of Manitoba
Winnipeg, MB, R3T 5V6, Canada
fangx@myumanitoba.ca

ABSTRACT

In this paper, direct numerical simulation (DNS) is performed to study the effects of the Coriolis force on turbulent heat transfer within a square duct subjected to spanwise system rotation. In order to investigate the rotation effects on the heat transfer process, a wide range of rotation numbers have been tested. In response to the system rotation, secondary flows appear as large streamwise counter-rotating vortices, which interact intensely with the four boundary layers of the square duct and have a significant impact on the statistics of the coupled velocity and temperature fields. It is observed that at sufficiently high rotation numbers, a Taylor-Proudman region appears and the flow approaches a complete laminarization state near the top and side walls. The influence of large organized secondary flows on the turbulent kinetic energy of the velocity field and turbulent scalar energy of the temperature field have been investigated through a spectral analysis. The effects of system rotation on the production of the temperature variance have been examined through a budget analysis of its transport equation.

INTRODUCTION

Turbulent heat transfer in a closed duct subjected to spanwise system rotation has many important industrial applications, such as turbine blade cooling and rotating heat exchangers. Pallares & Davidson (2002) conducted large-eddy simulation (LES) to study turbulent heat transfer in stationary and spanwise rotating square ducts under different wall heating conditions and Grashof numbers. They observed significant variation of Nusselt numbers with different boundary conditions (constant wall temperature or heat flux) and showed that turbulent intensity was strongly influenced by centrifugal buoyancy effect. Later, Pallares *et al*. (2005) further extended their LES studies to higher rotation number cases. They investigated the influences of secondary flow on the overall heat transfer performance and observed increased local Nusselt numbers on the unstable wall compared to the non-rotation case.

Thus far, transient simulation of turbulent heat transfer in a spanwise rotating square duct has been limited to only several LES studies as reviewed above. Application of DNS to this type of research has so far focused only on the turbulent flow field in the literature. Dai *et al.* (2015) conducted a DNS study of a spanwise rotating square duct flow. Through a careful examination of the budget balance of the mean momentum equations, they demonstrated the influence of secondary flows on turbulence statistics obtained at different rotation numbers. Very recently, Fang *et al*. (2017) performed DNS of spanwise rotating square duct flows at very high rotation numbers. They observed that the Coriolis force dominates the transport of Reynolds stresses and turbulent kinetic energy (TKE), and forces the spectra of streamwise and vertical velocities to synchronize within a wide range of turbulence scales.

For turbulent heat transfer within a spanwise rotating channel, the transport processes of momentum and thermal energy are coupled, and the physical mechanism is complicated not only by the two Coriolis force components induced by the system rotation but also by the presence of four solid side walls of the square duct. Currently, detailed DNS study of this special subject is still lacking in literature. In view of this, we aim at conducting a comprehensive comparative DNS study of the turbulent heat and fluid flow confined within a square duct subjected to spanwise system rotations, with a wide range of rotation numbers varying from $Ro_\tau = 2\Omega\delta/u_\tau = 0$ (corresponding to the non-rotating state) to $Ro_\tau = 18$ (which is the highest rotation number of the current literature). Here, u_τ is the wall friction velocity, δ represents half the channel height, and Ω denotes the angular speed of the spanwise system rotation. Also as our research objectives, the first- and second-order statistical moments of the velocity and temperature fields will be examined, the spectral characteristics of the TKE and temperature fluctuations will be studied, and the physical mechanisms underlying the interactions of the large secondary flow structures with the four boundary layers developed along the four walls of the square duct will be investigated.

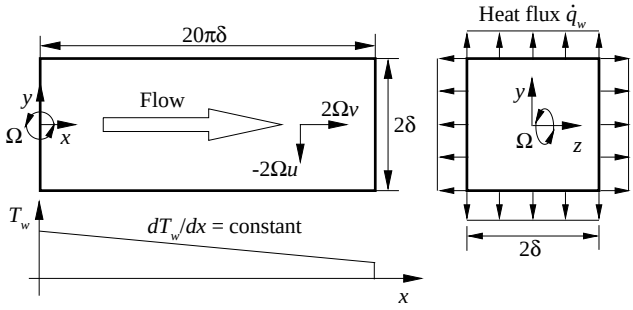

Figure 1. Side and front views of the computational domain and coordinate system. The two Coriolis force components in the rotating reference frame are $2\Omega v$ and $-2\Omega u$. The flow in the duct is cooled along the streamwise direction by imposing a constant wall heat flux on all four walls.

TEST CASES AND NUMERICAL ALGORITHM

Figure 1 shows the computational domain and coordinate system of the test case. The flow is confined within a closed square duct with the cross-sectional area $L_y \times L_z = 2\delta \times 2\delta$. Following Fang *et al.* (2017), in order to ensure the TKE associated with the most energetic eddies to be well captured in the streamwise direction, a very long square duct is used, with its streamwise computational domain size set to $L_x = 20\pi\delta$.

Both the flow and temperature fields are assumed to be fully developed and the periodic boundary conditions are applied to the

inlet and outlet of the duct. No-slip boundary condition is imposed on all four walls for the velocity field. The temperature field is assumed to be a passive scalar. A constant wall heat flux is imposed on all four walls of the square duct. The Prandtl number of the fluid is assumed to be 1.0 and the Reynolds number is fixed to $Re_\tau = u_\tau \delta/\nu = 150$. In order to examine the rotation effect, in total, eight rotation numbers are tested for $Ro_\tau = 0$, 0.25, 0.5, 2.5, 4.5, 9.0, 12.0 and 18.0.

In the spanwise rotating reference frame, the continuity, momentum and thermal energy equations for an incompressible flow can be expressed as

$$\frac{\partial u_i}{\partial x_i} = 0 \quad , \tag{1}$$

$$\frac{\partial u_i}{\partial t} + \frac{\partial}{\partial x_j}(u_i u_j) = -\delta_{1i}\Pi - \frac{1}{\rho}\frac{\partial p}{\partial x_i} + \nu\frac{\partial^2 u_i}{\partial x_j \partial x_j} + 2\varepsilon_{ij3}\Omega u_j \quad , \tag{2}$$

$$\frac{\partial T}{\partial t} + \frac{\partial}{\partial x_j}(u_j T) = -u_1\frac{dT_w}{dx} + \alpha\frac{\partial^2 T}{\partial x_j \partial x_j} \quad , \tag{3}$$

respectively. Here, coordinates x_1, x_2 and x_3 correspond to x, y and z, respectively, as in Fig. 1, and velocity components u_1, u_2 and u_3 are also denoted as u, v and w, respectively. In Eq. (3), $T_w = T_w(x)$ represents the local mean peripheral temperature over the wall at a given streamwise location. In the above equation, ρ, p, ν and α represent the density, pressure, kinematic viscosity and thermal diffusivity of the fluid, respectively, and ε_{ijk} and δ_{ij} are the Levi-Civita and Kronecker symbols, respectively. In Eqs. (2) and (3), Π and dT_w/dx are constant, representing the streamwise pressure and wall-temperature gradients, respectively. Given the fact that the duct flow is both hydraulically and thermally fully developed and is cooled down steadily under the constant surface heat flux condition, the discharge of thermal energy from the flow to the ambient environment occurs steadily along the streamwise direction. In consequence, both the bulk mean temperature and the local peripheral temperature of the wall decrease linearly in the streamwise direction, i.e. $dT_b/dx = dT_w/dx = 2\dot{q}_w/(\rho C_p U_b \delta)$. This further allows us to apply a periodical boundary condition to the temperature field in the streamwise direction, if the linear streamwise distribution of the bulk mean temperature is explicitly subtracted from the temperature field. In effect, in Eq. (3), T denotes the temperature deviation from the local bulk mean temperature, and $T + (dT_w/dx)x$ is the actual local temperature. This treatment method for the temperature field is similar to that used in the LES study of Pallares *et al.* (2005).

DNS is conducted using an open-source spectral-element method code (so-called "Semtex") originally developed by Blackburn & Sherwin (2004) for calculation of turbulent velocity fields. In order to perform heat transfer calculation, an additional thermal energy equation is implemented in Semtex by the authors with the same spectral accuracy. The computer code is developed using C++ and FORTRAN programming languages and parallelized using message passing interface libraries. Fourier series are used in the homogeneous streamwise direction, and the quadrilateral spectral-element method based on high-order Gauss-Lobatto-Legendre Lagrange interpolants is employed in the cross-stream directions. The time integration is achieved by utilizing the high-order splitting method proposed by Karniadakis *et al.* (1991).

In total, the current DNS uses $960 \times 129 \times 129$ grid points in the streamwise, vertical and spanwise directions, respectively. The cross-section of the duct is divided into 16×16 rectangular elements. The values of y^+ and z^+ of the first grid off the walls are below 0.4 in all tested cases. All simulations are conducted using a 240-core local computer cluster.

In this paper, the temperature field is non-dimensionalized using the wall friction temperature defined as $T_\tau = \dot{q}_w/\rho C_p u_\tau$, where C_p represents the specific heat of the fluid. The non-dimensionalized temperature is expressed as $\theta = (T - T_w)/T_\tau$. In presenting the results, a pair of angular brackets $\langle\cdot\rangle$ are used to denote averaging both in time and over the homogeneous streamwise direction. As such, the mean temperature is denoted as $\langle\theta\rangle$, and the instantaneous temperature can be decomposed as $\theta = \langle\theta\rangle + \theta'$.

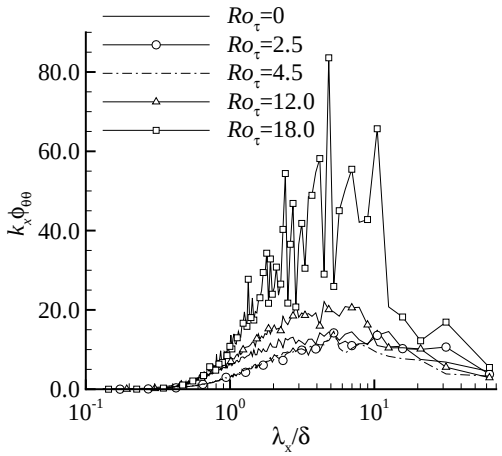

Figure 2. Pre-multiplied temperature spectra $k_x\phi_{\theta\theta}$ of different rotation numbers at position $(y/\delta, z/\delta)$=(0, -0.9).

RESULTS AND DISCUSSIONS

In order to validate that the streamwise computational domain size ($L_x = 20\pi\delta$) is long enough to resolve turbulent coherent structures of the temperature field, Fig. 2 compares the pre-multiplied spectra $k_x\phi_{\theta\theta}$ at five rotation numbers. Here, k_x and λ_x denote the wavenumber and wavelength in the streamwise direction, respectively. As seen in the figure, in all the plotted cases, the magnitude of $k_x\phi_{\theta\theta}$ at the largest resolved streamwise length scale is much smaller than its peak value. This indicates that the streamwise computational domain in current DNS is sufficiently long such that the turbulent scalar energy associated with different scales of flow motions are very well captured.

Figure 3 compares the streamlines of the mean velocity field and contours of $\langle\theta\rangle$ in the y-z plane at four different rotation numbers. From the figure, secondary flow appears as four pairs of counter-rotating vortices in each corner of the duct in the non-rotating case. In contrast, the pattern of secondary flow appears as a pair of counter-rotating vortices occupying the entire cross-section at $Ro_\tau = 18$. The peak value of $\langle\theta\rangle$ in the rotating case occurs at the vertical location below the duct center around $y/\delta = -0.5$. This is due to the downwash of the mean flow caused by the secondary flow associated with the system rotation. For detailed discussion of the velocity field, the reader is referred to Fang *et al.* (2017).

In order to compare the heat transfer performance, the Nusselt number is calculated as $Nu = \frac{1}{\langle\theta\rangle_b}\int_\Gamma \frac{\partial\langle\theta\rangle}{\partial n} d\Gamma$, where n and Γ denote the wall-normal direction and four peripheries of the cross-section of the square duct, respectively, and $\langle\theta\rangle_b$ represents the non-dimensional bulk mean temperature. Figure 4 shows the variations of the friction velocity and Nusselt number at different walls with the rotation number. In the figure, superscripts $(\cdot)^t$, $(\cdot)^s$ and $(\cdot)^b$ denote the value of a quantity on the top, side and bottom walls, respectively. It is well-known that for a zero-pressure-gradient heated turbulent boundary layer developed over a solid smooth still flat plate, the following analogy between velocity and temperature wall laws hold in the viscous sublayer, i.e., $u^+ = y^+$ and $\theta = Pr \cdot y^+$ (cor-

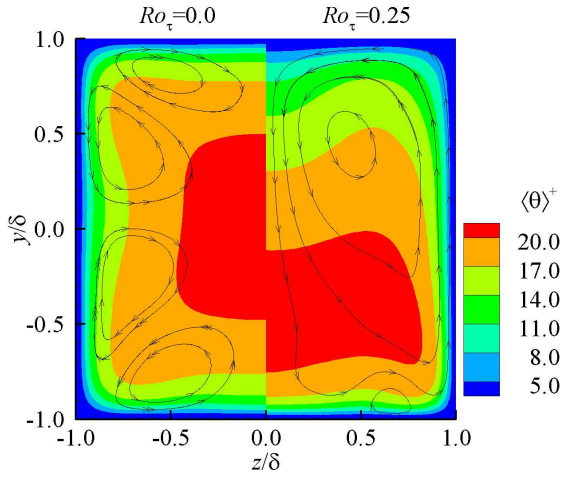

(a) The $Ro_\tau = 0$ and 0.25 cases

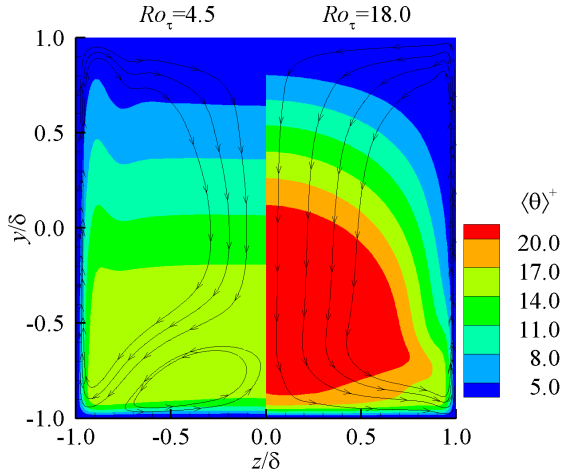

(b) The $Ro_\tau = 4.5$ and 18.0 cases

Figure 3. Time averaged cross-stream streamlines superimposed with contours of $\langle\theta\rangle$ for different rotation numbers.

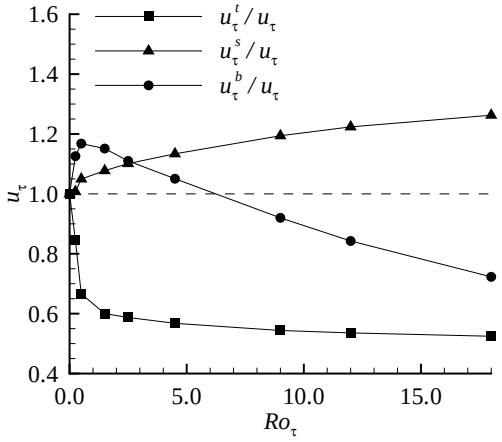

(a) Friction velocity

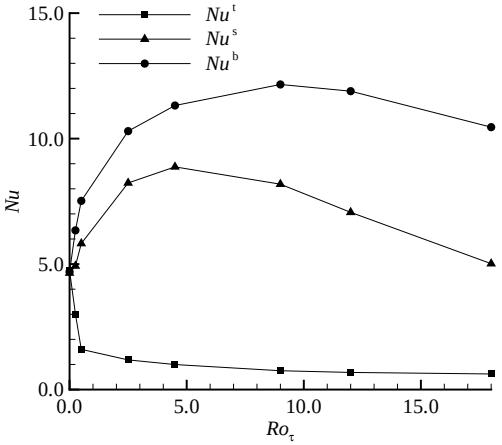

(b) Nusselt number

Figure 4. The variation of the friction velocity and Nusselt number at different duct walls with the rotation number.

respondingly, $\partial\langle\theta\rangle/\partial n = Pr\cdot\partial\langle u\rangle/\partial n$ and $Nu \propto Pr\cdot u_\tau^2$). This indicates that a large (small) Nusselt number relates to a large (small) wall friction velocity. The appearance the Coriolis forces as a result of system rotation has a significant impact on the transport processes of the momentum and thermal energy. As a result, such analogy between molecular diffusion processes of the momentum and thermal energy within the viscous sublayer holds only when the Coriolis force effects are negligible, and breaks as the rotation number increases. Indeed, based on their LES study of spanwise rotating square duct flow, Pallares & Davidson (2002) showed that this analogy holds approximately at low rotation numbers for $0 < Ro_\tau < 0.75$. The rotation number range tested here and in our previous study (Fang *et al.*, 2017) is the widest in literature. Our DNS results show that as Ro_τ increases larger than 0.75, the trend of the Nusselt number becomes inconsistent with that of the wall friction velocity. For instance, as seen in Fig. 4, the friction velocity at the bottom wall (u_τ^b) peaks between $Ro_\tau = 0.5$ and 1.5, however, the value of Nu^b increases monotonically within the rotation number range of $0 \le Ro_\tau \le 9$. It is interesting to see from Fig. 4(b) that the value of Nu^t shows a sharply decreasing trend for $0 \le Ro_\tau \le 0.5$, whereas Nu^t remains almost unchanged for $2.5 \le Ro_\tau \le 18.0$. This can be reasoned from the fact that the flow near the top wall becomes laminarized for $Ro_\tau \ge 2.5$ (Fang *et al.*, 2017) and, consequently, turbulent heat transfer is diminished.

Figure 5 compares the vertical profiles of $\langle u\rangle^+$ and $\langle\theta\rangle$ at different rotation numbers in the central plane ($z/\delta = 0$), respectively. As seen in Fig. 5(a), the value of $\langle u\rangle^+$ decreases monotonically as the rotation number increases. In contrast, from Fig. 5(b), it is interesting to observe that the variation of $\langle\theta\rangle$ with the rotation number exhibits a non-symmetrical and non-monotonic pattern. More specifically, for $0 \le Ro_\tau \le 2.5$, the magnitude of $\langle\theta\rangle$ within the upper half duct (for $0 < y/\delta < 1$) decreases as the rotation number increases. In contrast, the level of $\langle\theta\rangle$ increases as Ro_τ further increases beyond 4.5.

It is known that a Taylor-Proudman (TP) region (in which the mean streamwise velocity does not vary along the axis of rotation, i.e., $\partial\langle u\rangle/\partial z \approx 0$) exists in both turbulent and laminar duct flows at a sufficiently high spanwise rotation number (Speziale, 1982; Fang *et al.*, 2017). The presence of the TP region is evident at higher rotation numbers. For instance, as shown vividly in Fig. 3(b), at $Ro_\tau = 4.5$, the TP region (as indicated by the temperature contours) dominates the center of the duct for $|z/\delta| < 0.7$. It should be indicated here that although a passive scalar is useful for indicating the fluid flow structures, its transport process is governed separately by the convection-diffusion equation (i.e., Eq. (3)) rather than the momentum equation itself. Therefore, the dispersion pattern of the passive thermal energy may differ from the dominant flow pattern resulted purely from the momentum system. As shown in Fig. 3(b), as Ro_τ continues to increase to 18, the TP region can no loner be effectively demonstrated by using the contours of $\langle\theta\rangle$. In order to fur-

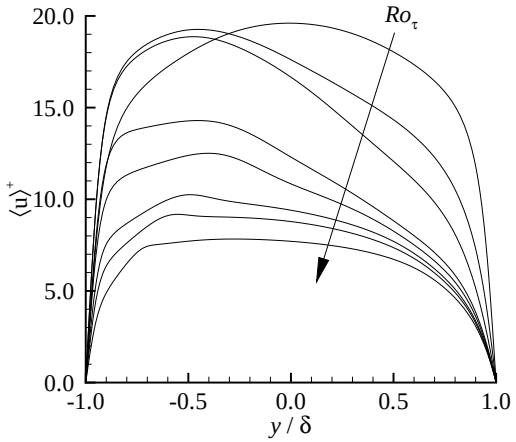

(a) Mean streamwise velocity $\langle u \rangle^+$

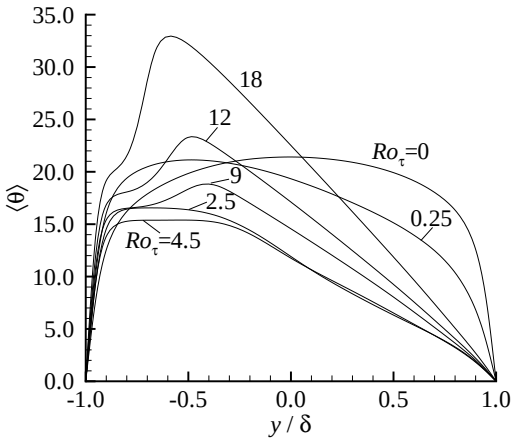

(b) Mean temperature $\langle \theta \rangle$

Figure 5. Vertical profiles of the non-dimensional mean streamwise velocity $\langle u \rangle$ and the mean temperature $\langle \theta \rangle$ of different rotation numbers in the central plane ($z/\delta = 0$). Arrow shows the monotonic variation of Ro_τ= 0, 0.25, 0.5, 2.5, 4.5, 9.0, 12.0 and 18.0.

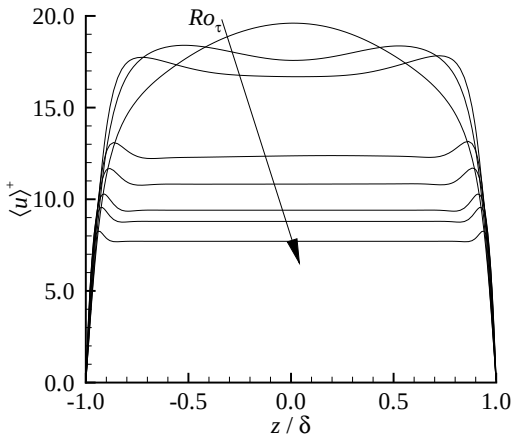

(a) Mean streamwise velocity $\langle u \rangle^+$

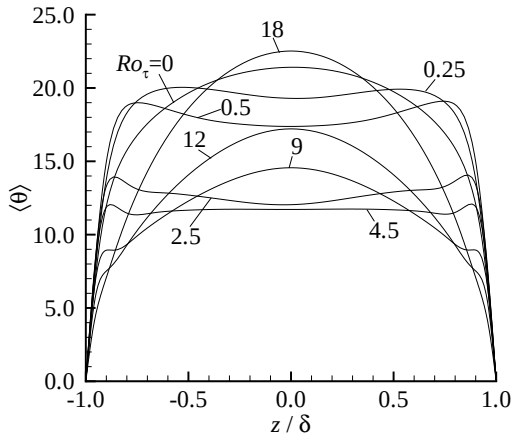

(b) Mean temperature $\langle \theta \rangle$

Figure 6. Spanwise profiles of the non-dimensional mean streamwise velocity $\langle u \rangle^+$ and the mean temperature $\langle \theta \rangle$ of different rotation numbers at half duct height ($y/\delta = 0$).

ther investigate the effect of system rotation on the transport of momentum and temperature, Fig. 6 shows the spanwise distributions of the mean velocity and temperature at different rotation numbers. As seen in Fig. 6(a), a TP region occurs at $Ro_\tau = 2.5$ and its spanwise extension increases monotonically as the rotation number further increases. In contrast, it is interesting to see in Fig. 6(b) that as the rotation number increases, the variation of $\langle \theta \rangle$ is non-monotonic. Specifically, the TP effect on the distribution of $\langle \theta \rangle$ is the strongest at $Ro_\tau = 4.5$ (which extends from $z/\delta = -0.8$ to 0.8), and weakens as Ro_τ further increases from 4.5 to 18.

Figures 7 (a) and (b) show the vertical profiles of TKE ($k = \langle u_i' u_i' \rangle / 2$) and temperature variance $\langle \theta' \theta' \rangle$ for different rotation numbers in the central plane ($z/\delta = 0$), respectively. It is evident from Fig. 7(a) that the turbulent intensity generally reduces as Ro_τ increases. Particularly, for cases of $Ro_\tau \geq 2.5$, the value of TKE in the upper half duct ($0 \leq y/\delta \leq 1$) is almost zero, which is an indication of laminarization over the top wall. Consequently, as seen in Fig. 7(b), the value of $\langle \theta' \theta' \rangle$ approaches zero in the laminarized region. It is also interesting to observe that the peak magnitude of $\langle \theta' \theta' \rangle$ increases as the rotation number increases beyond 2.5.

Figure 8 compares the vertical profiles of turbulent heat fluxes $\langle u' \theta' \rangle$ and $\langle v' \theta' \rangle$ at different rotation numbers in the central plane ($z/\delta = 0$). From Fig. 8(a), the value of $\langle u' \theta' \rangle$ monotonically decreases as the rotation number increases in general. In contrast, it is interesting to see in Fig. 8(b) that the peak magnitude of $\langle v' \theta' \rangle$ increases as the rotation number increases with the peak location fixed around $y/\delta = -0.9$. Although both velocity and temperature fluctuations are suppressed individually by system rotation close to the bottom wall (see Fig. 7), Fig. 8(b) suggests that the correlation between v' and θ' near the bottom wall is actually enhanced as the rotation number increases. To further understand this interesting observation, the transport equation of turbulent heat flux $\langle u_k' \theta' \rangle$ can be studied, which reads

$$\begin{aligned} &\underbrace{\langle u_j \rangle \frac{\partial \langle u_k' \theta' \rangle}{\partial x_j}}_{H_k} \underbrace{+ \langle u_j' u_k' \rangle \frac{\partial \langle \theta \rangle}{\partial x_j} + \langle u_j' \theta' \rangle \frac{\partial \langle u_k \rangle}{\partial x_j}}_{P_k^c} \\ &\underbrace{+ \frac{\langle u_1' u_k' \rangle}{T_\tau} \frac{dT_w}{dx_1}}_{P_k^s} \underbrace{+ \frac{\partial \langle u_j' u_k' \theta' \rangle}{\partial x_j}}_{D_k^t} \underbrace{- 2\varepsilon_{kj3} \Omega \langle u_j' \theta' \rangle}_{C_k} \\ &\underbrace{- \alpha \langle \frac{\partial^2 \theta'}{\partial x_j \partial x_j} u_k' \rangle - \nu \langle \frac{\partial^2 u_k'}{\partial x_j \partial x_j} \theta' \rangle}_{V_k} \underbrace{+ \langle \frac{\partial p'}{\partial x_k} \theta' \rangle}_{P_k} = 0 \quad . \end{aligned} \tag{4}$$

Here, H_k, D_k^t and V_k are the convection, turbulent diffusion and molecular diffusion-dissipation terms, respectively. P_k^c and P_k^s represent the turbulent production and turbulent production term due to the streamwise mean temperature gradient, respectively. P_k de-

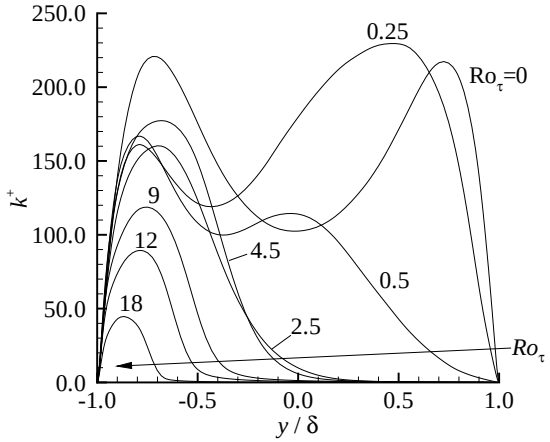

(a) TKE k^+

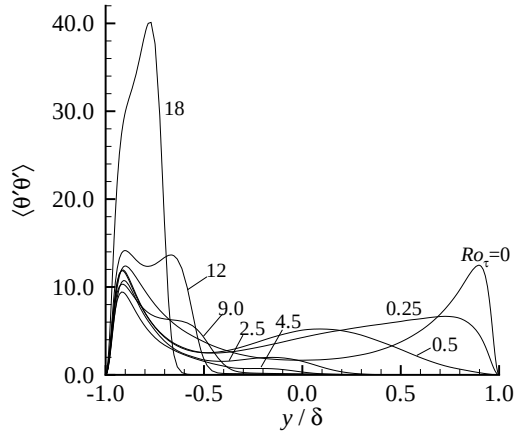

(b) Temperature variance $\langle\theta'\theta'\rangle$

Figure 7. Vertical profiles of TKE (k) and temperature variance $\langle\theta'\theta'\rangle$ of different rotation numbers in the central plane ($z/\delta = 0$).

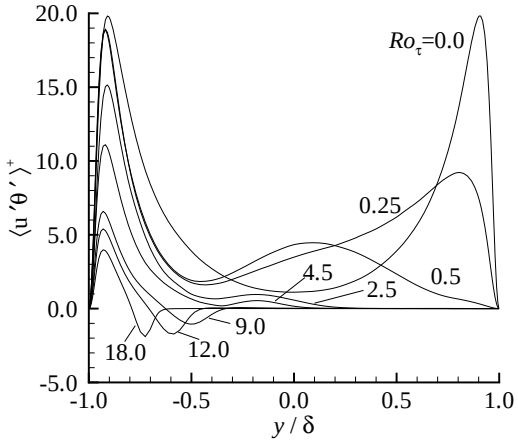

(a) Streamwise turbulent heat flux $\langle u'\theta'\rangle^+$

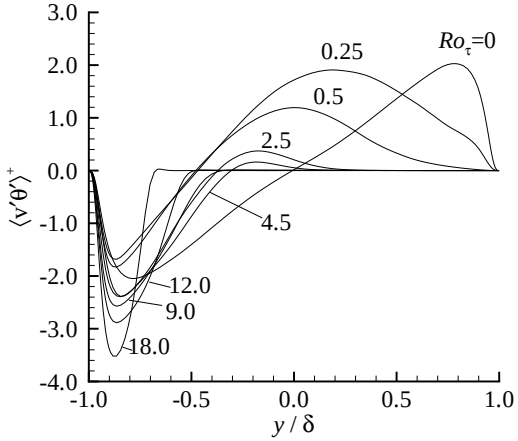

(b) Vertical turbulent heat flux $\langle v'\theta'\rangle^+$

Figure 8. Vertical profiles of turbulent heat fluxes $\langle u'\theta'\rangle^+$ and $\langle v'\theta'\rangle^+$ of different rotation numbers in the central plane ($z/\delta = 0$).

notes the pressure diffusion-redistribution term. The Coriolis production term C_k is introduced by the system rotation. It is worthy to note that it relates $\langle u'\theta'\rangle$ to $\langle v'\theta'\rangle$ because $C_1 = -2\Omega\langle v'\theta'\rangle$ and $C_2 = 2\Omega\langle u'\theta'\rangle$.

From Fig. 8(b), for cases of $Ro_\tau \geq 2.5$, the value of $\langle v'\theta'\rangle$ is negative in most of the turbulent regions near the bottom wall. Therefore, C_1 is positive and, consequently, destructs $\langle u'\theta'\rangle$. In other words, system rotation tends to suppress the level of $\langle u'\theta'\rangle$. In contrast, positively-valued $\langle u'\theta'\rangle$ near the bottom wall leads to positively-valued C_2 and, consequently, enhances $\langle v'\theta'\rangle$. Figure 9 compares the vertical profiles of the budget balance of $\langle v'\theta'\rangle$ for the non-rotating ($Ro_\tau = 0$) and rotating ($Ro_\tau = 2.5$) cases at $z/\delta = 0$. It is interesting to see that the Coriolis production term C_2 becomes dominant in the budget balance of $\langle v'\theta'\rangle$ at $Ro_\tau = 2.5$ and its peak location is consistent with that of $\langle v'\theta'\rangle$ shown in Fig. 8(b). In other words, system rotation tends to increase the magnitude of $\langle v'\theta'\rangle$. This explains the observation in Fig. 8(b) that the magnitude of $\langle v'\theta'\rangle$ increases near the bottom wall as the rotation number increases.

It is well known that the Taylor-Görtler (TG) vortices appear as streamwise-elongated counter-rotating roll cells in spanwise-rotating turbulent plane-channel flows (Johnston *et al.*, 1972; Kristoffersen & Andersson, 1993). As demonstrated previously in Fang *et al.* (2017) by using streamwise velocity spectra and here in Fig. 2 by using the streamwise temperature spectra, we confirm that such streamwise elongated structures also exist in a spanwise-rotating square duct flow. To further investigate, Fig. 10 displays a typical instantaneous fluctuating temperature fields around the roll cells in a cross-section plane at $Ro_\tau = 12.0$. To clearly demonstrate the flow structures, only a portion of the domain ($-1 \leq z/\delta \leq 0$ and $-1 \leq z/\delta \leq -0.4$) is plotted. From Fig. (10), two pairs of counter-rotating roll cells can be observed and, ejection events (featuring positively-valued v') occur between vortices. As a consequence, near-wall fluid with low temperature is convected upwards and negatively-valued θ' is generated. As such, a large magnitude of $\langle v'\theta'\rangle$ is maintained at high rotation numbers, a pattern that can be clearly observed in Fig. 8(b).

CONCLUSIONS

Direct numeric simulation (DNS) is conducted to investigate turbulent heat transfer in a closed square duct subjected to spanwise rotation. The rotation numbers tested here are among the highest in literature. The effects of system rotation on the turbulent flow and temperature fields are examined in terms of the mean temperature, Nusselt number, turbulent heat fluxes, streamwise temperature spectra, and the budget balance of the transport equation of turbulent heat fluxes.

Induced by the Coriolis forces, secondary flows appear as streamwise-elongated counter-rotating vortex pairs in the cross-section direction. A Taylor-Proudman region appears in the center of the duct, which has a profound influence on the dispersion of

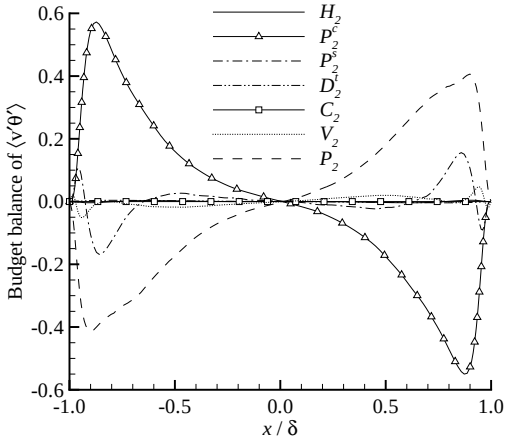

(c) Budget balance of $\langle v'\theta'\rangle$ for $Ro_\tau = 0$

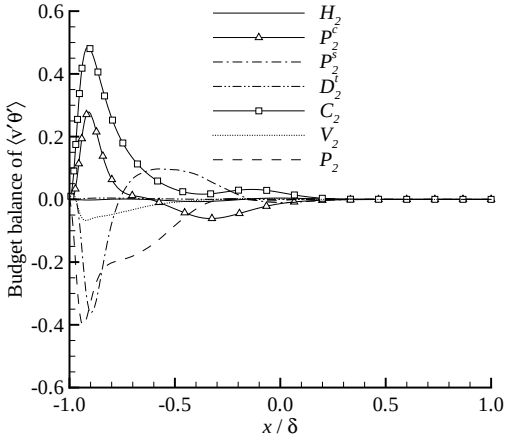

(d) Budget balance of $\langle v'\theta'\rangle$ for $Ro_\tau = 2.5$

Figure 9. Budget balance of $\langle v'\theta'\rangle$ in the central plane ($z/\delta = 0$) at $Ro_\tau = 0$ and 2.5. All the budget terms are non-dimensionalized using u_τ^2/δ.

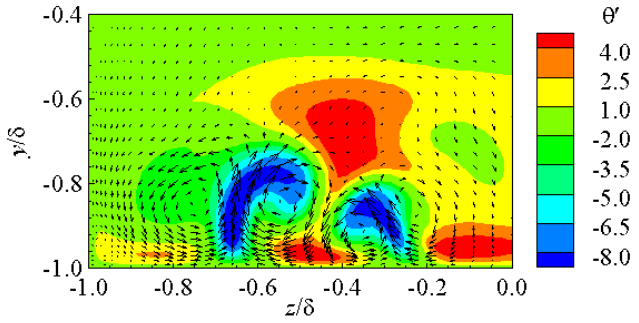

Figure 10. Contours of instantaneous temperature fluctuation θ' superimposed with vectors of fluctuating velocities (w', v') in a portion (for $-1 \le z/\delta \le 0$ and $-1 \le y/\delta \le -0.4$) of cross-section (z-y) plane at $Ro_\tau = 12.0$.

the thermal energy. The investigation of Nusselt number at different walls shows that the analogy between the molecular diffusion processes of the momentum and thermal energy within the viscous sublayer (typical of a zero-pressure-gradient boundary layer developed over a solid smooth wall) holds only when the Coriolis force effects are negligible, and breaks as the rotation number increases.

Both the velocity and temperature fluctuations (as indicated by TKE and temperature variance $\langle\theta'\theta'\rangle$) become suppressed as the rotation number increases in general. However, it is interesting to observe that the magnitude of the vertical turbulent heat flux ($\langle v'\theta'\rangle$) increases as the rotation number increases. By investigating the budget balance of the transport equation of $\langle v'\theta'\rangle$, it is concluded that system rotation tends to enhance $\langle v'\theta'\rangle$ through the Coriolis production term which relates to the streamwise turbulent heat flux $\langle u'\theta'\rangle$. Furthermore, by analyzing the turbulent structures in the cross-stream plane, it is observed that the ejection events pump near-wall cold fluid upwards to sustain the level of negatively-valued vertical turbulent heat flux $\langle v'\theta'\rangle$.

REFERENCES

Blackburn, H. M. & Sherwin, S. J. 2004 Formulation of a Galerkin spectral element-Fourier method for three-dimensional incompressible flows in cylindrical geometries. *J. Comp. Phys.* **197(2)**, 759–778.

Dai, Y. J., Huang, W. X., Xu, C. X. & Cui, G. X. 2015 Direct numerical simulation of turbulent flow in a rotating square duct. *Phys. Fluids* **27**, 065104.

Fang, X., Yang, Z., Wang, B.-C. & Bergstrom, D. J. 2017 Direct numerical simulation of turbulent flow in a spanwise rotating square duct at high rotation numbers. *Int. J. Heat Fluid Flow*, in press.

Johnston, J. P., Halleen, R. M. & Lezius, D. K. 1972 Effects of spanwise rotation on the structures of two-dimensional fully developed turbulent channel flow. *J. Fluid Mech.* **56(3)**, 533–557.

Karniadakis, G. E., Israeli, M. & Orszag, S. A. 1991 High-order splitting methods for the incompressible Navier-Stokes equations. *J. Comp. Phys.* **97(2)**, 414–443.

Kristoffersen, R. & Andersson, H. I. 1993 Direct simulations of low-Reynolds-number turbulent flow in a rotating channel. *J. Fluid Mech.* **256**, 163–197.

Pallares, J. & Davidson, L. 2002 Large-eddy simulations of turbulent heat transfer in stationary and rotating square ducts. *Phys. Fluids* **14(8)**, 2804–2816.

Pallares, J., Grau, F. X. & Davidson, L. 2005 Pressure drop and heat transfer rates in forced convection rotating square duct flows at high rotation rates. *Phys. Fluids* **17**, 075102.

Speziale, C. G. 1982 Numerical study of viscous flow in rotating rectangular ducts. *J. Fluid Mech.* **122**, 251–271.